LINEAR ACTUATOR OF ELECTROMAGNETIC SUSPENSION OPTIMIZATION BASED ON MULTI-OBJECTIVE PARTICLE SWARM ALGORITHM

Chao Yang[1,2,*], ZhiYuan Qu[1,2], ShuYang Li[1], TianYu Xu[1], LanXin DengMu[1]
[1]College of Automotive and Traffic Engineering, Henan Polytechnic, Zhengzhou 450056, China
[2]Henan Engineering Research Center of Intelligent Vehicle Emission Detection and Control, Zhengzhou 450056, China

Abstract - An analytical model of the linear actuator's magnetic field is first constructed in order to examine and mitigate the impact of electromagnetic thrust ripple on the linear actuator of the electromagnetic active suspension system. The study of the induced voltage in relation to the electromagnetic force output provides a total harmonic distortion (THD) of 8.4%. THD is utilised as the evaluation index for the harmonic content in the induced voltage. Based on this, the vehicle dynamic reaction characteristics are examined and a suspension system control model that takes electromagnetic thrust ripple characteristics into account is established. The multi-objective particle swarm optimisation approach is utilised to accomplish the multi-objective optimisation for the two objectives, "small THD" and "large induced voltage amplitude," using the actuator's parameters. The optimum is then chosen from the Pareto optimal solution set using fuzzy set theory. According to the modelling results, it is possible to efficiently enhance the electromagnetic force by 7.9% and decrease the electromagnetic thrust ripple by 55.8%. The efficacy of the electromagnetic thrust ripple analysis and optimisation described in this research is finally verified by testing the actuator prototype.

Keywords: Electromagnetic active suspension; Linear actuator; Electromagnetic thrust ripple; Multi-objective optimization; Multi-objective particle swarm optimization (MOPSO).

1. Introduction

Ride comfort and handling stability cannot be balanced by conventional suspension technologies. By using an electromagnetic active suspension to provide adjustable active suspension forces, this conflict can be resolved [1-3]. As one of the main parts of the electromagnetic active suspension, electromagnetic dampers—especially permanent-magnet dampers with high power density—have been researched too little to far. The effectiveness of electromagnetic active suspensions and their application in the intelligent chassis of electric vehicles depend on these dampers' characteristics.

Currently, the research on electromagnetic dampers primarily focuses on two types of dampers: linear actuators and rotary actuators [4]. In order to provide the damper electromagnetic damping force, rotary actuators, which consist of a rotating motor and a mechanism, are used to transform the rotary motion, such as a ball screw [5] or rack and pinion [6]. However, the system stability is further weakened by the transmission chain's length, low transmission efficiency, comparatively high motion inertia, and the power transmission mechanism's gear meshing's propensity to loosen.

Linear actuators are tiny gears with simple structure and high gearbox efficiency. It allows for mitigating the gearbox mechanism and use direct drive to generate electromagnetic force to meet the suspension damping force need [7]. Based on the electromagnetic induction concept, Alhams et al. [8] created a magnetic induction actuator. Nevertheless, the induction actuators require current to wind the excitation magnetic field since they lack a permanent magnetic field. Under the same power, induction actuators have a larger input current, which leads to severe overheating and reduced efficiency. The "path of least reluctance" principle, which states that magnetic flux is always steered down the path of lowest reluctance without the need for any windings to produce the excitation magnetic field, is the basis for how SR actuators operate. Compared to induction actuators, they feature a simpler structure and a

dx.doi.org/10.17683/ijomam/issue25/v1.8

higher working efficiency [9]. An active suspension system utilising a low-cost, high-performance linear switching reluctance actuator (LSRA) is presented by Lin et al. [10]. However, these actuators have a large magnetic force shock in the electromagnetic force output due to the doubly salient structural design [11]. Conversely, permanent-magnet actuators, which use permanent magnets (NdFeB) as the source of the magnetic field, are more efficient and have a higher power density. In contrast to switching reluctance actuators, permanent-magnet actuators (PMAs) are a good option for electromagnetic suspension actuators because of their singly salient or non-salient structure design, which can lessen electromagnetic force shock. Wang et al. [12] investigated such actuators and created magnetic circuit analysis formulas and magnetic field simulation models, providing the theoretical foundation for permanent-magnet actuator design. Additionally, research was conducted on the impact of leading design factors on the drive system and performance of a tubular permanent magnet machine [13], as well as its use in automobiles [14]. Tran et al. [15] created a permanent-magnet actuator for motorcycles that delivers greater power density and efficiency by using NdFeB permanent magnets to generate the magnetic field.

A three-phase permanent-magnet linear active suspension actuator was created and tested on a BMW vehicle by Gysen et al. [16] of Eindhoven University of Technology. The findings showed that the vehicle's wheel dynamic load dropped by 54% and its sprung mass acceleration dropped by 36%, which improved the vehicle's handling stability and ride comfort [17].

Nevertheless, the majority of research on these actuators has overlooked the electromagnetic thrust ripple caused by the slot structure, end effects, and magnetic field harmonics. These factors have an adverse effect on the precise output of the electromagnetic force and thus present a challenge when designing the suspension controller.

In order to minimise electromagnetic thrust ripple from the perspective of optimal pole-slot matching, fractional-slot designs were used in the design of electromagnetic suspension actuators based on the aforementioned analysis [18]. In order to develop a skewed-tooth and skewed-pole structure to lessen electromagnetic thrust ripple, it altered the forms of the stator teeth and the mover permanent magnets, focusing on the process of how these shapes effect electromagnetic force [19]. In order to minimise the electromagnetic thrust ripple, the ideal mover length was calculated from the end force point of view, taking into consideration the actuator's end effects [20].

The electromagnetic thrust ripple analysis of the linear actuator for electromagnetic active suspension is carried out in this study from the perspective of induced voltage harmonics. This is used to create an active suspension dynamic model and analyse how the electromagnetic thrust ripple affects active suspension performance. From the perspective of the actuator body design, a multi-objective particle swarm intelligent optimisation algorithm is used to optimise the structural parameters of the electromagnetic active suspension linear actuator in order to reduce electromagnetic thrust ripple and increase the effective electromagnetic force output of the linear actuator. This eliminates the impact of actuator electromagnetic thrust ripple on the active suspension performance. Lastly, actuator bench testing confirm the actuator's optimised design.

2. Electromagnetic Active Suspension Actuator

2.1 Actuator Structure

The active suspension actuator created in this paper is of the permanent-magnet linear kind. Figure 1 depicts the installation scheme in the drive wheel of an electric car. The vehicle frame is the sprung mass, and the wheel axle, hub and tyre are the unsprung masses to which the main body is attached. The coils are wound on the primary core, and the permanent magnets are positioned on the secondary core. Road excitation generates induced current in the winding coils and moves the primary and secondary cores in relation to one another. In order to reduce vibrations and recover vibration energy, this current will create an electromagnetic damping force in the magnetic field. Additionally, three-phase alternating current can actively generate electromagnetic force in the actuator, which can stabilise the vehicle's running attitude, improve driving safety, and provide lateral support force to the vehicle in challenging operating conditions.

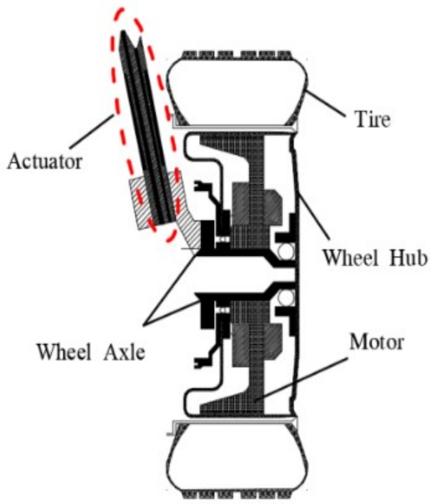

Figure 1: Installation of the actuator on the vehicle

The actuator is set up to have a cylinder-like exterior form. The actuator's winding coefficient is increased and its cogging force is reduced by using a fractional-slot arrangement with 12 slots and 14 poles. DW465-50 silicon steel sheets are used to make the actuator's laminated primary and secondary cores. The permanent magnet is made of NdFeB (NdFe30), which has a coercivity of 838 kA/m, a remanent flux density of 1.1 T, and winding coils made of copper wire with a diameter of 1 mm.

To satisfy the actuator's stroke requirements and make it simple to attach the actuator on the vehicle, the major core's outer radius is 42 mm and its length is 174 mm. The ideal ratio was found to be 0.55 based on the analysis of how the secondary outer diameter to primary outer diameter ratio of the linear motors affected the electromagnetic force [13]. In this paper, a ratio of 0.5 is chosen based on slot size and ease of winding coil installation. The air gap should be 2 mm long, and slots with a flat bottom should be utilised. The higher winding coefficient is used to increase the actuator's power density. Lastly, the armature is a three-phase double-layer winding structure, and a 12-slot, 14-pole fractional-slot construction is used for this paper. Figure 2 depicts the actuator's structure, while Table 1 lists its dimensions.

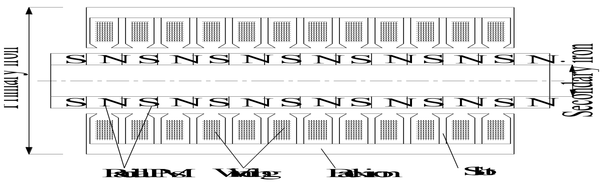

Figure 2: Configuration of the 12-slot 14-pole the actuator

Table 1. Design parameters of the 12-slot/14-pole the actuator

Number	Item	Unit	Value
1	Slot height/h_w	mm	17
2	Slot pitch/τ_s	mm	14
3	Slot width/τ_w	mm	6
4	PM length/τ_m	mm	12
5	PM height/h_m	mm	3
6	Notch width/b_0	mm	3
7	The number of turns in each slot	—	100
8	The primary outer radius/R_s	mm	42
9	The primary inner radius/R_i	mm	22
10	The secondary outer radius/R_m	mm	20
11	The secondary inner radius/R_r	mm	17
12	The primary length/L_p	mm	174
13	Air gap length/g	mm	2

3. Model Establishment and Validation

3.1 Analytical Model of the Actuator's Induced Voltage

One of the primary characteristics that can be monitored to ascertain the electromagnetic force production of the electromagnetic actuators is the induced voltage. Figure 3 illustrates the analytical model of the induced voltage that must be constructed in order to analyse the actuator's performance in this study.

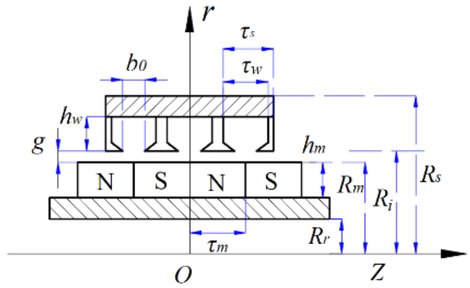

Figure 3: Structural parameters of the actuator

Because this work uses an open-slot actuator stator, leakage of the air-gap magnetic flux affects the induced voltage of the actuator. With reference to the reference [14], the impact of the slot opening is considered and the Carter coefficient Kc is incorporated in order to precisely compute the damper's induced voltage. Formula (1) displays its expression:

$$K_C = \frac{\tau_s}{\tau_s - \gamma g'} \tag{1}$$

Where, $g' = g + h_m / \mu_r$, τ_s is the slot pitch; g is the air gap length; μ_r is the relative permeability of the permanent magnet, taken as 1.04; h_m is the permanent magnet thickness. The formula for the slot opening factor γ is shown in Formula (2):

$$\gamma = \frac{4}{\pi}\{\frac{b_0}{2g'}\tan^{-1}(\frac{b_0}{2g'}) - \ln\sqrt{1+(\frac{b_0}{2g'})^2}\} \tag{2}$$

Where, b_0 is the slot opening width.

The effective air gap length g_e and the effective primary radius R_{se} are expressed shown in Formula (3) and Formula (4), respectively:

$$g_e = g + (K_C - 1)g' \tag{3}$$

$$R_{se} = R_m - g_e \tag{4}$$

Where, R_m is the inner radius of the permanent magnet. At the effective primary radius R_{se}, Formula (5) illustrates how to determine the flux linkage of a single-phase winding at the effective primary radius by calculating the magnetic flux density with respect to the coil pitch:

$$\Psi = \sum_{n=1,2\cdots}^{\infty} \psi_{np} \cos m_n (z - \tau_{cp}/2) \tag{5}$$

Where, τ_{cp} is the coil pitch (in this study, the actuator pitch τ_{cp} equals the tooth pitch τ_s); ψ_{np} is the n-th harmonic flux linkage coefficient, as shown in Formula (6):

$$\psi_{np} = \frac{4\pi p N_c K_{dpn}}{m_n} K_{rn} \tag{6}$$

Where, N_c is the number of coil turns per pole per phase; K_{dpn} is the winding coefficient; p is the number of pole pairs; m_n refers to the n-th harmonic angular frequency; and K_{rn} is the magnetic field distribution factor, as shown in Formula (7):

$$K_{rn} = R_{se}[a_{1n} BI_1(m_n R_{se}) + b_{1n} BK_1(m_n R_{se})] \tag{7}$$

Where, BI_1 and BK_1 are the first-order modified Bessel functions of the first and second kind, respectively. The single-phase winding induced voltage E is obtained by differentiating the flux linkage from Equation (5) with respect to time, as shown in Formula (8):

$$E = \frac{d\Psi}{dt} = v \sum_{n=1,2\cdots}^{\infty} 4\pi p N_c K_{dpn} K_{rn} \sin m_n (z - \tau_{cp}/2) \tag{8}$$

Where, v is the actuator operating speed.

3.2 Analysis of the Actuator's Electromagnetic Force

Depending on the speed and current, the electromagnetic suspension's electromagnetic force can be adjusted in real time. The actuator's electromagnetic force can be expressed as follows in Formula (9) if the current excitation is applied:

$$F = \frac{P}{v} = \frac{E_A I_A + E_B I_B + E_C I_C}{v} \tag{9}$$

Where, P is the actuator input power; E_A, E_B, and E_C refer to the three-phase induced voltages; and I_A, I_B, and I_C represent the three-phase currents.

When a three-phase AC current with the same phase as the three-phase induced voltage is applied to the analytical expression of the induced voltage in Equation (8), the electromagnetic force can be produced.

PWM voltage harmonics are introduced by an inverter in practical applications, which unavoidably cause current distortion and increase ripple force. The simulation in this paper is predicated on an ideal sinusoidal current stimulation.

$$\text{Phase A} \quad I_{A\max} \sin(\omega t - 2\pi/3 + \phi) \tag{10}$$

$$\text{Phase B} \quad I_{B\max} \sin(\omega t + \phi) \tag{11}$$

$$\text{Phase C} \quad I_{A\max} \sin(\omega t + 2\pi/3 + \phi) \tag{12}$$

Where, I_{max} is the peak value of each phase current; the current angular frequency $\omega = 2\pi f$; f is the current frequency; and ϕ is the initial phase angle. (See Formulas 10-12).

In order to confirm the accuracy of the model, a finite element model of the actuator was also created in the Ansoft Maxwell electromagnetic simulation program, as seen in Figures 4 and 5.

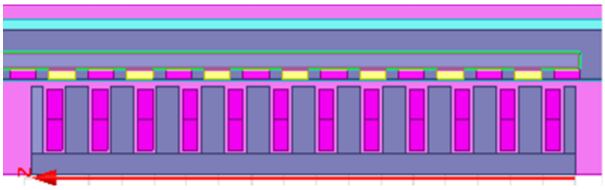

Figure 4: Finite element model of the actuator

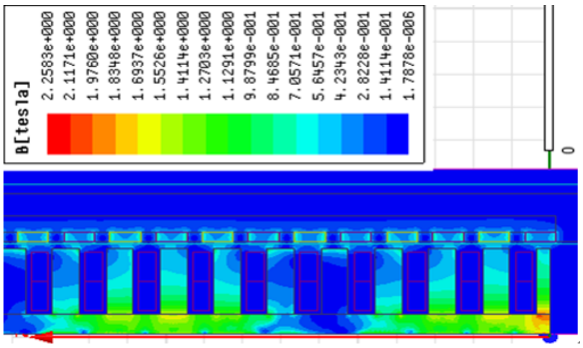

Figure 5: Magnetic flux density distribution contour diagram of the actuator

3.3 Results Analysis

Figures 6 and 7 depict the actuator's air-gap magnetic flux density and single-phase induced voltage, respectively. Figure 6 shows that there is generally good agreement between the theoretically derived values (analytical model, AM) and finite element analysis (FEA) values of the actuator's air-gap magnetic flux density throughout one pole length.

Figure 7 makes it clear that the induced voltage distribution is almost sinusoidal. Figure 8 displays the actuator's electromagnetic force output characteristics at 0.12 m/s and 3 A input current. It is evident that the actuator's electromagnetic force output fluctuates periodically, with a maximum value of -168.3 N, a minimum value of -134.8 N, and a ripple of 33.5 N.

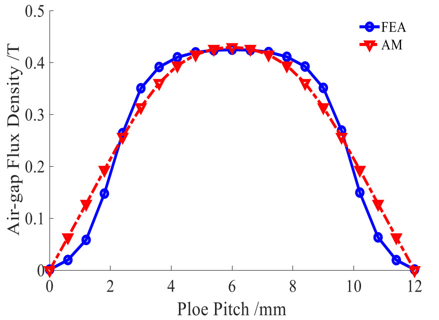

Figure 6: Air-gap flux density of the actuator over one pole pitch

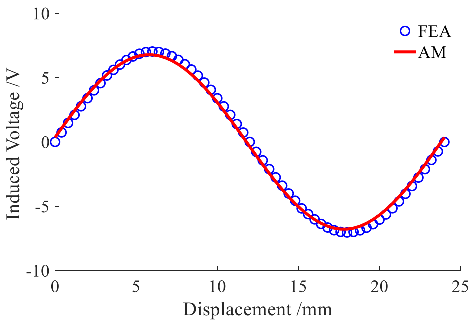

Figure 7: Induced voltage of the actuator over one pole-pair pitch

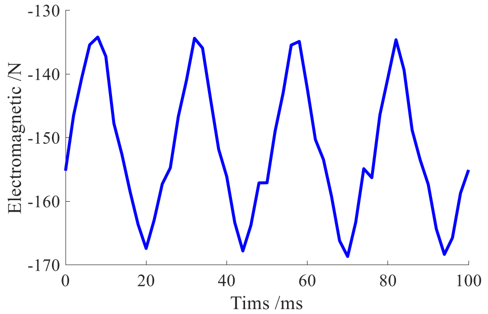

Figure 8: Electromagnetic force of the actuator

These variations cause mistakes in the electromagnetic force produced and may also cause vibrations in the suspension assembly's structural components, which ultimately compromises the system's dependability. They must therefore be sufficiently suppressed.

4. Induced Voltage Harmonic Analysis

Equation (8) reveals: These harmonics cause the electromagnetic force to ripple when they are mixed with the input three-phase currents. Since the current excitation employed in the simulation is an ideal sine wave, the optimisation of electromagnetic thrust ripple in this article focuses on examining the harmonics in the actuator's induced voltage. The total harmonic distortion (THD), as indicated in Formula (13), can be used to characterise the harmonic content of the actuator's induced voltage:

$$THD = \sqrt{\sum_{n=2}^{n} (\frac{G_n}{G_1})^2} \times 100\% \tag{13}$$

Where, G_n is the RMS value of the *n*-th harmonic component, G_1 is the RMS value of the fundamental component and *n* is the specified order. Here, n is taken up to 8 because the ratio of the higher order harmonics to the fundamental is somewhat small. Based on calculations, the THD of the actuator's induced voltage is around 8.4%.

It is evident that the structural characteristics of the actuator are the primary elements influencing the harmonic content of the induced voltage when this expression is combined with the analytical formulation of the induced voltage in Equation (8). The permanent magnet pole arc coefficient αρ, the width of the slot τw, the thickness of the permanent magnet hm, and the length of the air gap g are the primary factors affecting the output of the permanent magnet motor if the actuator's length, number of poles, number of slots, and number of winding turns remain constant. Figure 9 shows the findings of a study on how each parameter affects the induced voltage's THD.

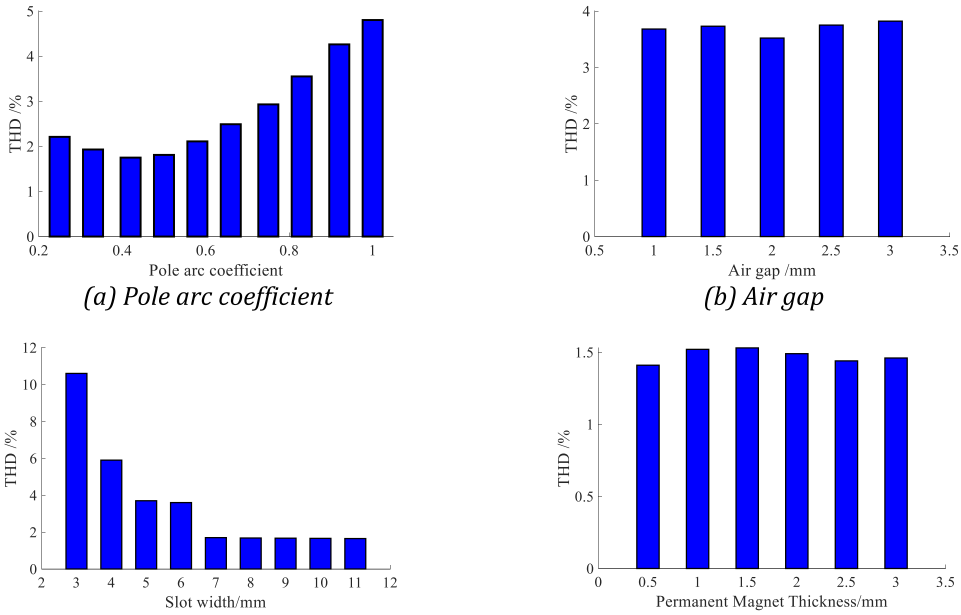

(a) Pole arc coefficient *(b) Air gap*

(c) Slot width *(d) Permanent magnet thickness*

Figure 9: Influence of various parameters on the THD of the induced voltage

Based on Figure 9, t the THD first decreases and then increases as the pole arc coefficient increases, with the lowest THD occurring at a pole arc value of roughly 0.4–0.5. Since the THD only minimally changes when both air gap length and permanent magnet thickness increase, their effects on the THD are not very noticeable.

The THD is relatively steady at a slot width of 7 mm and decreases rather quickly as the slot width increases. Nevertheless, each parameter simultaneously modifies the induced voltage's amplitude Em and THD. Here, each parameter's impact on Em is examined, and Figure 10 displays the findings.

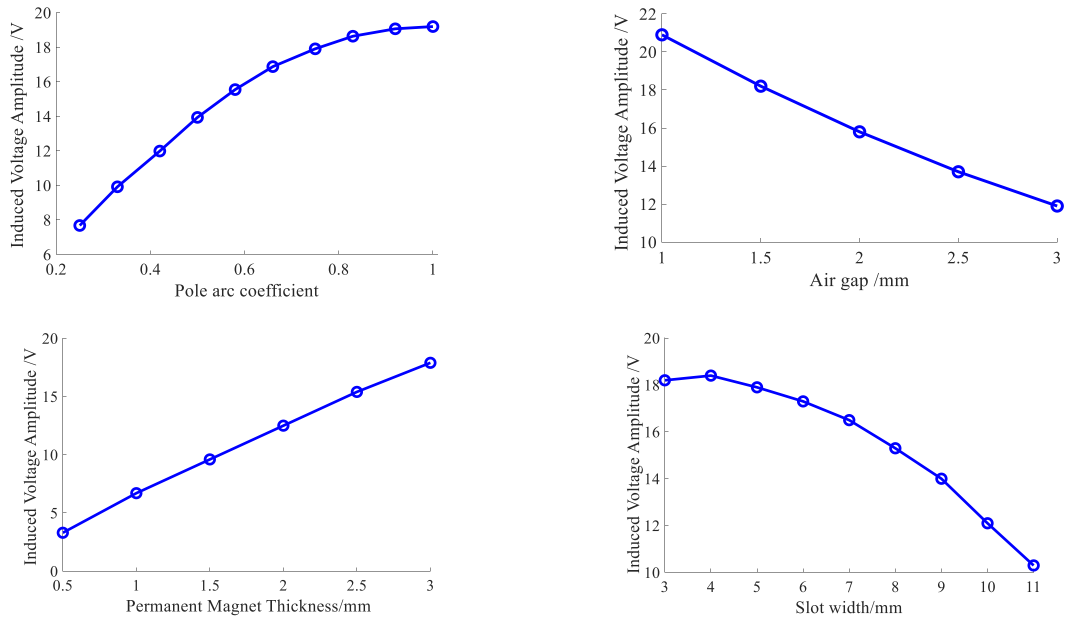

Figure 10: Influence of various parameters on the amplitude of the induced voltage

As seen in Figure 10, the induced voltage amplitude Em rises with the pole arc coefficient and permanent magnet thickness but gradually falls with air gap length and slot width. This is mainly due to the fact that greater Em will be produced at the actuator's air gap with larger permanent magnet pole arc coefficients and thicker magnets. Conversely, increasing the air gap and slot width will reduce the air-gap magnetic flux density and the effective magnetic flux that passes through the teeth, which will lower Em.

5. Active Suspension Characteristics Considering Electromagnetic Thrust ripple

5.1 Active Suspension Dynamic Model

In summary, the electromagnetic actuator's output force has a specific periodicity rather than a set value. These variations affect the dynamic performance and the efficacy of the active control of the electromagnetic active suspension and cause errors in the electromagnetic force production. This work provides an active suspension dynamic model that takes electromagnetic thrust ripple into account in order to analyse its impact on the system.

The actuator output model, which takes electromagnetic thrust ripple into account, and the quarter-vehicle dynamic model, as depicted in Figure 11, make up the two halves of the active suspension dynamic model. The sprung mass (Ms) and unsprung mass (Mu), the suspension's stiffness (K_3) and damping (C_3), the tire's stiffness (K_1), the sprung mass's displacement (Zs), the unsprung mass's displacement (Zu), the road's excitation (Zg), the active control force (Fa), and the constant (Ke), which excludes the ripple term, are the parameters in this instance.

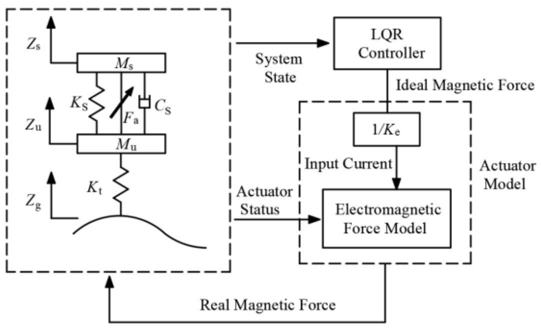

Figure 11: Control system block diagram of the active suspension considering electromagnetic thrust ripple

The fundamental concept of the system simulation is as follows, as shown in Figure 11: the LQR active controller determines the input current of the actuator without the ripple force and computes the theoretical control force required by the suspension system. An actual output electromagnetic force of the actuator with ripple is obtained along with the actuator's operational state. In order to apply this actual output electromagnetic force as the active control force to the vehicle system, it is used as Fa.

The parameters of the actuator's operating state and the input current must be determined in order to determine the ripple electromagnetic force output of the actuator. The actuator's operating speed and relative location are examples of its operating state parameters. The vehicle dynamics model and the actuator's installation form in the suspension indicate that the actuator's relative displacement is $\dot{Z}_u - \dot{Z}_s$ and its operation speed is $\dot{Z}_u - \dot{Z}_s$.

Formula (14) expresses the electromagnetic actuation force while neglecting harmonic components:

$$F = 3 I_m K_e \tag{14}$$

Where, K_e is the constant ignoring harmonic components, I_m is the actuator input current, and F is the theoretical control force output by the LQR controller.

In conclusion, the input current Im, the actuator's speed $\dot{Z}_u - \dot{Z}_s$ and its displacement can be used to determine the actual output force of an actuator with an electromagnetic thrust ripple. The real electromagnetic force that the actuator $Z_u - Z_s$ produces is known as the suspension system's active control force F_a.

Table 2 lists the active suspension controller's and the suspension system simulation model's parameters. Table 1 lists the actuator's structural parameters. The simulation model uses a Class Broad, and the vehicle's speed is set at 72 km/h.

Table 2: Parameters of the suspension model and controller

Parameter	Value
Sprung mass M_s/kg	310
Unsprung mass M_u/kg	70
Suspension stiffness K_3/(N/m)	27358
Suspension damping Cs/(N/(m/s))	984
Tyre stiffness K_1/(N/m)	309511
Controller parameter $q1$	$1×10^5$
Controller parameter $q2$	$1×10^6$
Controller parameter $q3$	$1×10^{10}$
Controller parameter r	0.01

5.2 Suspension System Response Analysis

Figure 12 displays the output time domain response of the suspension system. The figure indicates that the peak value of each vibration peak rises and that the electromagnetic thrust ripple has an impact on the sprung mass acceleration, the dynamic deflection of suspension, and the wheel hop. Table 3 displays the RMS value for the aforementioned three parameters. Based on the response curves in the time domain in Figure 12, it is evident that the vibration acceleration of the sprung mass, the dynamic deflection of the suspension, and the wheel hop are increased by 5.16%, 4.76%, and 4.55%, respectively. Overall, the actuator has an impact on performance, and appropriate steps should be taken to remove this impact.

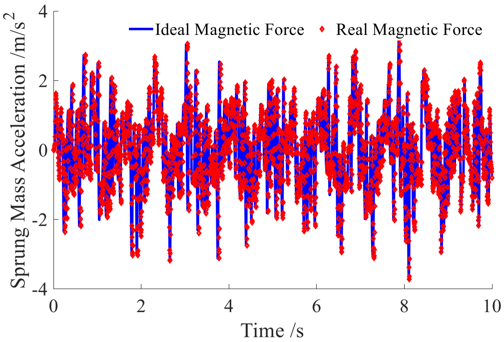

(a) Vertical acceleration of the vehicle sprung mass

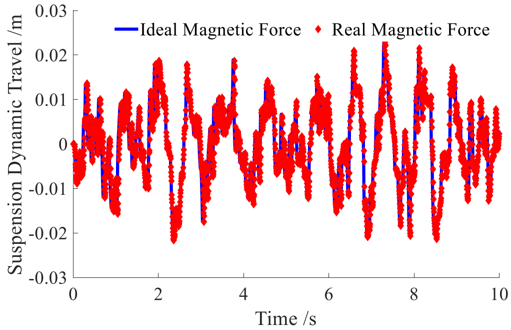

(b) Suspension dynamic travel

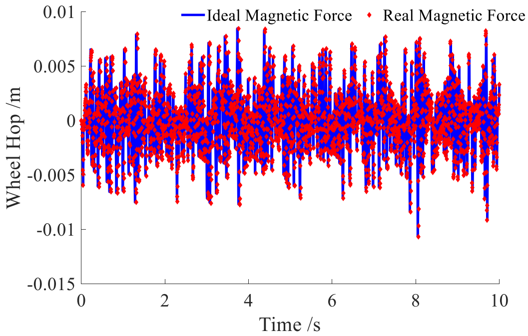

(c) Wheel hop

Figure 12: Time-domain response of the suspension system output

Table 3: Comparison of the time-domain response RMS values

Parameters/unit	Theoretical control effect	Actual control effect	Change amplitude (%)
Sprung mass acceleration/(m/s^3)	0.8675	0.9123	5.16↑
dynamic deflection of suspension /m	0.0063	0.0056	4.76↑
Wheel hop/m	0.0022	0.0023	4.55↑

6. Actuator Optimization Based on Multi-Objective Particle Swarm Optimization

The description above makes clear that the electromagnetic thrust ripple affects the suspension system's dynamic performance to some extent. The more effective the electromagnetic force, the less of an impact it has on the suspension system's dynamic performance. In this work, the structural characteristics of the actuator are optimised from an actuator design perspective using the multi-objective particle swarm optimisation (MOPSO) technique based on Pareto dominance relationships.

The actuator optimization problem can be expressed as follows if it is considered a multi-objective nonlinear ptimization problem with n ptimization objectives and u constraint conditions:

$$F_{fitness}(x)=best\{f_1(x), f_2(x), \cdots f_n(x)\} \quad x\in T \tag{15}$$

$$T=\{x\in R^m,\ G: g_{i\min}\le g_i(x)\le g_{i\max},\ i=1,\cdots,u\} \tag{16}$$

Where, $f_1(x)$, $f_2(x)$, ..., $f_n(x)$ are the 1st to n -th optimization design objectives; T denotes the constraint conditions; R^m is the design variable domain; *G* denotes the variable constraints; *n* stands for the design objective dimension; *m* denotes the design variable dimension; and *u* is the number of constraints (See Formula 15-16).

6.1 Design Objectives

In order to decrease the electromagnetic thrust ripple, the actuator's structural parameters should be optimised. On the other hand, the amplitude Em of the induced voltage should be increased in order to increase the effective electromagnetic force output. Therefore, the n value for the design objective dimension in this work is 2. The design objective functions used are as follows.

Objective function 1

$$f_1(x) = E_m \tag{17}$$

Objective function 2

$$f_2(x) = THD \tag{18}$$

The optimisation algorithm's particle selection procedure adheres to the "large Em, small THD" approach (see Formula 17-18).

6.2 Design Variables and Constraints

According to the effects of the structural parameters of the actuator on the THD and the amplitude E_m of the induced voltage, the permanent magnet pole arc coefficient α_p, the slot width τ_w, the permanent magnet thickness h_m and the air gap *g* are chosen as the design variables, that is, the design variable dimension is *m*= 4. The range of values of α_p, τ_w, h_m and *g* is determined based on tooth strength, avoiding magnetic saturation, and non-interference of primary and secondary motion.

The design variable and constraints are as follows.

Design variable is:

$$x = [\alpha_p, \tau_w, h_m, g]$$

Constraints:

$$\alpha_p \in [0.3, 0.8] \quad \tau_w \in [4.0, 14.0]$$

$$h_m \in [2.5, 5.0] \quad g \in [1.5, 2.0]$$

Despite the fact that the design variables are continuous, a lower bound on the minimum permitted air gap length must be imposed due to the manufacturing process requirements for actuator installation accuracy [21] and the need to mitigate structural risks that could arise from an excessively small air gap length [22]. As a result, the minimum air gap length is set at 1.5 mm and the resolution of all parameters is set to 0.1 mm during the optimisation process.

6.3 Multi-Objective Particle Swarm Optimisation Algorithm

When using multi-objective optimisation in the actuator, the multi-objective particle swarm optimisation technique is the best option to prevent issues with local optima and competing objectives in multi-objective allocation. This study uses an adaptive penalty function multi-objective stochastic particle swarm optimisation algorithm and the linear inertia weight coefficient modification method to obtain more real Pareto solutions, improving the algorithm's global search capability. The algorithm's adaptive penalty function is primarily made up of the multiplication of constraint violations and a changeable multiplication factor:

$$p(t, x) = \sqrt{t}\sum_{t=1}^{m}\theta(d_i(x))d_i(x)^{r(d_i(x))} \tag{19}$$

Where, *t* is the number of iterations; *m* represents the number of constraint conditions; and the penalty is determined by the order of magnitude of the objective function and the degree of penalty (See Formula 19).

6.4 Optimisation Results Analysis

In this research, the amplitude of the induced voltage and the THD of the actuator are taken into account when optimising the structural parameters of the actuator using a multi-objective particle swarm optimisation approach. The linear weight coefficient spans from 0.4 to 0.9, and the generic learning factors *C1*=*C2*=2 are utilised in the optimisation process. The size of the search space determines the maximum velocity, V_{max}:

$$V_{\max} = \lambda |x|_{\max} \tag{20}$$

Where, λ is the proportionality coefficient between the maximum velocity and the position limit (See Formula 20).

The population size is 50 and λ is set to 0.1 for the actuator. After 200 iterations, the structural parameters of the suspension actuator yield the Pareto optimal solution set, as shown in Figure 13.

The Pareto solution set contains a collection of non-dominated solutions, as Figure 13 illustrates. It demonstrates that when E_m rises, THD rises as well. This is paradoxical, and the solution that satisfies the condition must be chosen from the collection of solutions. Choosing the optimal option from the set is therefore especially crucial.

6.5 Pareto Solution Selection Based on Fuzzy Set Theory

Many subjective elements are involved in the traditional manual selection of Pareto solutions. The fuzzy set theory is used in this paper to select a Pareto solution [17]. Decision-makers can effectively choose Pareto solutions using a fuzzy mechanism thanks to fuzzy set theory, which adopts a compromise approach to optimal solution schemes. Formula (21) illustrates the membership function S_i^j:

$$S_i^j \begin{cases} 1 & f_i^j \le f_i^{\min} \\ \dfrac{f_i^{\max} - f_i^j}{f_i^{\max} - f_i^{\min}} & f_i^{\min} \le f_i^j \le f_i^{\max} \\ 0 & f_i^j \ge f_i^{\max} \end{cases} \tag{21}$$

Where, $f_i^{\max}$ and $f_i^{\min}$ are the maximum and minimum values of the *i*-th optimization objective in the solution set, respectively; f_i^j and S_i^j are the current value and membership value of the *i*-th optimization objective for the *j*-th solution.

The dominance function is defined, and the dominance value of the k-th solution is expressed as shown in Formula (22):

$$\varphi_k = \sum_{i=1}^{n} S_i^k \Big/ \left(\sum_{j=1}^{l}\sum_{i=1}^{n} S_i^j\right) \tag{22}$$

Where, *l* is the number of solutions in the external set — based on the simulation results of the model, *l* is taken as 14; and *n* refers to the number of suspension optimization design objectives, taken as 2.

Based on the formula of calculating the dominance function φ_k, the value of the dominance function of every non-dominated solution in the Pareto solution set can be acquired. The solution with the highest dominance value is selected as the best one since it reflects the solution's overall performance. As seen in Figure 14, the fourth particle individual has the highest values of the dominance function. Table 4 presents the actuator design variables' final values as well as their values before to and following optimization.

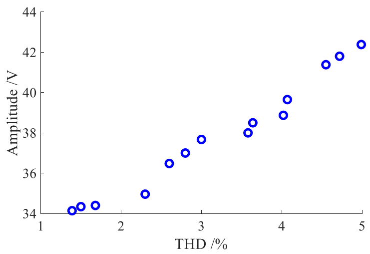

Figure 13: Pareto optimal solution

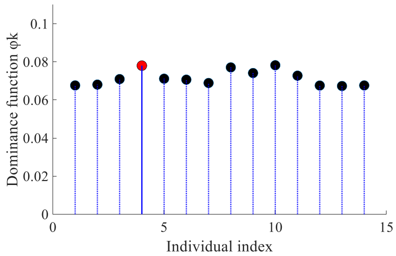

Figure 14: Dominance function of the Pareto optimal solutions

Table 4: Design variables before and after optimization

Design Parameters/unit	Before optimization	After optimization
Permanent magnet thickness hm/mm	4.0	4.5
Air-gap length g/mm	2.0	1.5
Pole arc coefficient αp/mm	0.9	0.7
Slot width τw/mm	6.0	10.0

6.6 Optimization Results Analysis

In order to compare the electromagnetic force of the actuator before and after optimisation, Table 4's structure parameters are used. When the running speed is 0.24 m/s, Figure 15 displays comparison curves of the winding induced voltage before and after optimisation. The induced voltage amplitude after optimisation is 8.6% greater than the one without optimisation.

Figure 16 displays the electromagnetic thrust ripple curves before and after optimisation under AC stimulation (exciting current = 3A). Following optimisation, the effective electromagnetic force rises by 7.9% and the electromagnetic thrust ripple falls by 55.8%. The actuator performance before and after optimisation on suspension dynamic performance is compared in Table 5. After optimisation, the sprung mass acceleration, suspension dynamic deflection, and wheel hop are closer to the theoretical optimal value, which enhances the suspension dynamic performance.

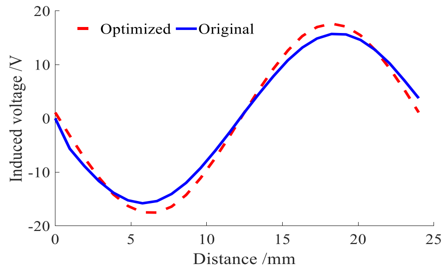

Figure 15: Comparison of Induced voltage

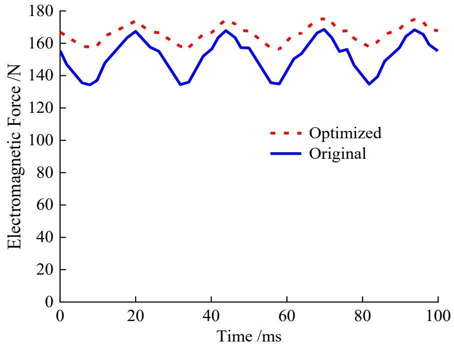

Figure 16: Comparison of electromagnetic forces

Table 5: Comparison of actuator parameter results

Parameters/unit	Original	Optimized	Theoretical optimum
Sprung mass acceleration / (m/s2)	0.9123	0.8742	0.8675
Suspension dynamic deflection /m	0.0066	0.0064	0.0063
Wheel hop /m	0.0023	0.0022	0.0022

7. Testing of Linear Actuator of Electromagnetic Suspension

Actuator prototype was produced after the design was used to determine the actuator' s optimal structural dimensions. The findings of the actuator structural optimisation were verified by testing the prototype's performance parameters.

The actuator was tested using a damper test bench, and its electromagnetic force and ripple tests were conducted using QC/T545-1999, the automotive telescopic damper bench test method.

The WDTS-IV damper extensive electrical dynamometer, computer, and fixtures make up the majority of the actuator's test apparatus. The primary technical specifications are as follows: 20 KN is the maximum excitation force; 80 mm is the maximum excitation amplitude; 1.2 m/s is the maximum simple harmonic motion speed; and 20 g is the maximum acceleration. The force sensor has a 10-10000N range. The induced voltage is shown using an SDS1102CN digital oscilloscope. An externally attached, adjustable disc-type load resistor. The test bench is displayed in Figure 17.

Figure 17: Bench test of the actuator

Before the damping force test, the prototype was positioned vertically on the test bench with the approximate center of the working stroke serving as the test stroke center. Figure 18 displays the results of plotting indication diagrams for one sample cycle under a ±25 mm stroke at maximum speeds of 0.1 m/s, 0.2 m/s, and 0.3 m/s using external adjustable resistances of 2 Ω, 4 Ω, and 8 Ω. The comparison of test values is displayed in Table 6.

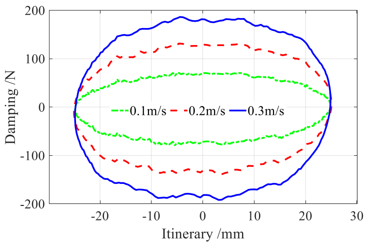

(a) Damping under 2 Ω load

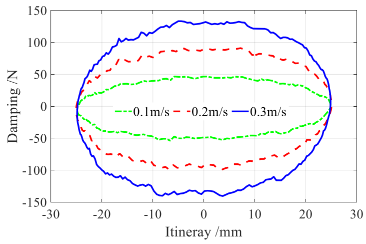

(b) Damping under 4 Ω load

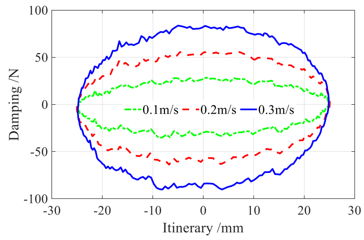

(c) Damping under 8 Ω load

Figure 18: Damping of the actuator

The damping force test curves in the aforementioned experiments show some oscillations, particularly around the top of the curves. Of these, Figure 18(a) has the greatest damping ripple force. The optimised electromagnetic thrust ripple (Table 6) has an amplitude of 11.6 N, 14.3 N, and 14.9 N at the identical speeds of 0.1 m/s, 0.2 m/s, and 0.3 m/s under the load of 2Ω. It is evident that every optimised test value is lower than the pre-optimization values. This confirms that the electromagnetic thrust ripple optimisation for the actuator described in this research is effective.

Table 6: Comparison of electromagnetic thrust ripple values under 2 Ω load

	Velocity/(m/s)	Test (Original)/N	Test (Optimized)/N	Amplitude/ %
Electromagnetic force ripple amplitude	0.1	11.6	3.8	67.2
	0.2	14.3	6.3	55.9
	0.3	14.9	7.1	52.3

8. Conclusions

This research focuses on the negative impact that the electromagnetic force ripple of a linear actuator with a 12-slot/14 pole design in active suspension has on the suspension system's dynamic characteristics. The four actuator structural parameters—tooth width, permanent magnet thickness, pole arc coefficient, and air gap length—have been optimised through the use of a multi-objective particle swarm intelligent optimisation technique. According to the experimental findings, the sprung mass vibration acceleration, the suspension dynamic deflection, and the wheel hop of the active suspension system all rose by 5.16%, 4.76%, and 4.55% when the actuator's electromagnetic force ripple was present. Following optimisation, the electromagnetic force output value increases by approximately 7.9% and the electromagnetic force ripple value decreases by approximately 55.8%. The regulation of the wheel hop, suspension dynamic deflection, and sprung mass acceleration for the active suspension system is closer to the ideal theoretical value. Additionally, the test results demonstrated the effectiveness of the optimisation strategy.

Furthermore, only the enhancement of the active suspension dynamic characteristic under the particular operating conditions was examined in this research. In the future, we will gradually integrate the suspension active and semi-active integrated control strategy with the complete vehicle dynamics model to confirm that the actuator in the vehicle's intelligent chassis system ensures the comfort, energy conservation, and safety.

Funding

This work is supported by the Key Research and Development Promotion Special Project (Science and Technology Research Project) of Henan Province (Grant No.232102240060).

References

[1] Xing, L., Kou, F., & Wang, G. (2025). Energy recovery and energy-saving control of a novel hybrid electromagnetic active suspension system for electric vehicles. *Energy*, 335. https://doi.org/10.1016/j.energy.2025.138030

[2] Tan, B., Tan, X., & Liu, J. (2025). Cooperative compensation control for a novel semi-active electromagnetic suspension integrating with variable damper and variable inertance. *Mechanical Systems and Signal Processing*, 226. https://doi.org/10.1016/j.ymssp.2025.112344

[3] Kim, S.-M., Kim, D. W., & Kwak, M. K. (2023). Design and implementation of an active vibration control algorithm using servo actuator control installed in series with a spring-damper. *Applied Sciences*, 13(5). https://doi.org/10.3390/app13053349

[4] Sun, D., Ding, R., & Dong, R. (2025). A review of linear motor electromagnetic energy regenerative suspension and key technologies. *Energies*, 18(19), 5158. https://doi.org/10.3390/en18195158

[5] Manca, R., Ruzimov, S., & Galluzzi, R. (2024). Enhancement of electromechanical load-leveling suspensions for automotive applications using reversible transmission mechanisms. *Mechatronics*, 102. https://doi.org/10.1016/j.mechatronics.2024.103229

[6] Hussain, S., YueDong, Z., & Raza, A. (2022). Power generating shock absorber for vehicles using thermopile. Paper presented at the *2022 International Conference on Emerging Trends in Electrical, Control, and Communication Systems (ETECCS)*, Jamshoro, Pakistan. https://ieeexplore.ieee.org/document/10068921

[7] Hu, Y., Li, Y., & Zheng, L. (2021). Analysis and suppression of in-wheel motor electromagnetic excitation of IWM-EV. *Proceedings of the Institution of Mechanical Engineers, Part D: Journal of Automobile Engineering*. https://doi.org/10.1177/0954407020979096

[8] Alhams, A., Qazak, A., & Badri, Y. (2024). Design and testing of a hybrid electromagnetic damping device for automotive applications. *Journal of Magnetism and Magnetic Materials*, 589. https://doi.org/10.1016/j.jmmm.2023.171606

[9] Baoming, G., Almeida, A. D., & Ferreira, F. (2009). Design of Transverse Flux Linear Switched Reluctance Motor. *IEEE Transactions on Magnetics*, 45(1), 113-119. https://doi.org/10.1109/TMAG.2008.2006193

[10] Lin, J., Cheng, K. W. E., & Zhang, Z. (2013). Active suspension system based on linear switched reluctance actuator and control schemes. *IEEE Transactions on Vehicular Technology*, 62(2), 562–572. https://doi.org/10.1109/TVT.2012.2222682

[11] Lin, J., Cheng, K. W. E., & Xue, X. (2012). Direct Instantaneous Force Control With Improved Efficiency for Four-Quadrant Operation of Linear Switched Reluctance Actuator in Active Suspension System *IEEE Transactions on Vehicular Technology*, 61(4), 1567–1575. https://doi.org/10.1109/TVT.2020.3008787

[12] Wang, J., & Howe, D. (2005). Tubular modular permanent-magnet machines equipped with quasi-Halbach magnetized magnets—Part I: Magnetic field distribution, EMF, and thrust force. *IEEE Transactions on Magnetics*, 41(9), 2470–2478. https://doi.org/10.1109/TMAG.2010.2096508

[13] Wang, J., & Howe, D. (2004). Design optimization of radially magnetized, iron-cored, tubular permanent-magnet machines and drive systems. *IEEE Transactions on Magnetics*, 40(5), 3262–3277. https://doi.org/10.1109/TMAG.2004.833424

[14] Wang, J., Wang, W., & Tuplin, S. (2010). Design and control of a linear electromagnetic actuator for active vehicle suspension. In *14th International Forum on Advanced Microsystems for Automotive Applications* (pp. 311–323). https://doi.org/10.1007/978-3-642-16362-3_30

[15] Tran, V. K., Han, P W., Chun, Y. D. (2022). Design of a 120 W Electromagnetic Shock Absorber for Motorcycle *Applications. Applied Sciences*, 22(17), 8688. https://doi.org/10.3390/app12178688

[16] Gysen, B. L. J., Paulides, J. J. H., Janssen, J. L. G., & Lomonova, E. A. (2010). Active electromagnetic suspension system for improved vehicle dynamics. *IEEE Transactions on Vehicular Technology*, 59(3), 1156–1163. https://doi.org/10.1109/TVT.2009.2038706

[17] Gysen, B. L. J., van der Sande, T. P. J., & Paulides, J. J. H. (2011). Efficiency of a regenerative direct-drive electromagnetic active suspension. *IEEE Transactions on Vehicular Technology*, 60(4), 1384–1393. https://doi.org/10.1109/TVT.2011.2131160

[18] Qian, W., & Jianbin, W. (2016). Assessment of cogging-force-reduction techniques applied to fractional-slot linear permanent magnet motors equipped with non-overlapping windings. *IET Electric Power Applications*, 10(8), 697–705. https://doi.org/10.1109/TIA.2018.2838528

[19] Zhu, Y., Lee, S., & Chung, K. (2009). Investigation of auxiliary poles design criteria on reduction of end effect of detent force for PMLSM. *IEEE Transactions on Magnetics*, 45(6), 2863–2866. https://doi.org/10.1109/TMAG.2009.2018778

[20] Inoue, M., & Sato, K. (2000). An approach to a suitable stator length for minimizing the detent force of permanent magnet linear synchronous motors. *IEEE Transactions on Magnetics*, 36(4), 1890–1893. https://doi.org/10.1109/20.877814

[21] Deng, Z. X., & Lai, F. (2011). Electromagnetic active vehicle suspension system. *In Proceedings - 3rd International Conference on Measuring Technology and Mechatronics Automation, ICMTMA* 2011(2), 15–18. https://doi.org/10.1109/ICMTMA.2011.291

[22] Nguyen, D. N., Deng, Z. X., Cao, Y. Q. (2011). Direct current linear actuator using in the active suspension system of automobile. *In 2011 International Conference on Electric Information and Control Engineering (ICEICE)*, 2011(7), 5855-5860. https://doi.org/10.1109/ICEICE.2011.5777281